Compressed Sensing-Based Inpainting of Aqua Moderate Resolution Imaging Spectroradiometer Band 6 Using Adaptive Spectrum-Weighted Sparse Bayesian Dictionary Learning

Huanfeng Shen, *Member, IEEE*, Xinghua Li, Liangpei Zhang, *Senior Member, IEEE*,
Dacheng Tao, *Senior Member, IEEE*, and Chao Zeng

***Abstract*— Because of malfunction or noise in 15 out of the 20 detectors, band 6 (1.628–1.652 μm) of the Moderate Resolution Imaging Spectroradiometer (MODIS) sensor aboard the Aqua satellite contains large areas of dead pixel stripes. Therefore, the corresponding high-level products of MODIS are corrupted by this periodic phenomenon. This paper proposes an improved Bayesian dictionary learning algorithm based on the burgeoning compressed sensing theory to solve this problem. Compared with other state-of-the-art methods, the proposed method can adaptively exploit the spectral relations of band 6 and other spectra. The performance of the proposed method is demonstrated by experiments on both simulated Terra and real Aqua images.**

***Index Terms*— Aqua Moderate Resolution Imaging Spectroradiometer (MODIS), band 6, Bayesian dictionary learning, compressed sensing (CS), image inpainting.**

I. INTRODUCTION

THE Moderate Resolution Imaging Spectroradiometer (MODIS) sensor aboard the Terra and Aqua satellites is a flagship of the primary sensors of the earth observation system project of National Aeronautics and Space Administration, with the former launched in December 1999 and the latter in May 2002. Moreover, the Terra satellite orbits the earth from north-to-south (descending), passing the equator at 10:30 A.M. local time, whereas the Aqua satellite passes in the opposite direction (ascending) over the equator at 1:30 P.M. zone time. As a result, they are making consecutive and compensative morning and afternoon observations of the land, ocean, and lower atmosphere as their respective launches. Each MODIS sensor, on both the Terra and Aqua satellites, senses the earth's surface by 36 spectral bands covering the wavelength from 0.415 (visible spectrum) to 14.235 μm [infrared (IR) spectrum] at three different nadir spatial resolutions: 250 (bands 1–2), 500 (bands 3–7), and 1000 m (bands 8–36) [1]. The bands of 250, 500, and 1000 m resolution have 40, 20, and 10 detectors per band, respectively [2].

Specifically, 15 of the 20 detectors of band 6 (1.628–1.652 μm) of the Aqua MODIS sensor are out of working as it was launched on May 4, 2002, meaning that their data are periodically missing or are so noisy as to be considered unusable [3]. However, MODIS band 6 is an important band that is used in various MODIS products and applications, including aerosol products, the normalized difference snow index, determination of cloud overlap, forest biomass estimation, and canopy water stress [1]. Recently, there are several research projects investigating this ongoing problem, the purpose of which is to recover the incomplete data. In addition, it is revealed that spectral correlation exists between Aqua MODIS band 6 and the other bands. Rakwatin *et al.* [1] proposed histogram matching, which corrects the detector-to-detector striping of the functional detectors, and local least squares fitting, which restores the missing data of the nonfunctional detectors according to the relationship between Aqua MODIS bands 6 and 7. Similarly, Shen *et al.* [4] proposed an algorithm called within-class local fitting (WCLF), based on the aforementioned two bands. Wang *et al.* [2] retrieved Aqua MODIS band 6 using another band, based on the relevance in Terra MODIS. However, these methods mainly exploit the relationships between bands 6 and 7, with the other spectral relations not being made use of. To obtain more information, Gladcova *et al.* [3] developed a new quantitative image restoration model utilizing the relationships between all seven bands of the 500-m resolution granules and implemented the recovery using multilinear regression. Above methods are based on the establishment of explicit relations between band 6 and the other bands.

In the digital image processing field, the process of retrieving the missing data in an image is known as image inpainting [5]. Up to now, many algorithms are used, such as interpolation [6], [7], partial differential equation [8], [9], total

---

Manuscript received July 20, 2012; revised January 11, 2013; accepted February 2, 2013. Date of publication March 22, 2013; date of current version December 12, 2013. This work was supported in part by the National Basic Research Program of China 973 Program under Grant 2011CB707103, the National Natural Science Foundation of China under Grant 41071269, and the Hubei Natural Science Foundation under Grant 2011CDA096.

H. Shen and X. Li are with the School of Resource and Environmental Science, Wuhan University, Wuhan 430079, China (e-mail: shenhf@whu.edu.cn; lixinghua5540@sina.com.cn).

L. Zhang and C. Zeng are with the State Key Laboratory of Information Engineering in Surveying, Mapping, and Remote Sensing, Wuhan University, Wuhan 430079, China (e-mail: zlp62@public.wh.hb.cn; zengchaozc@hotmail.com).

D. Tao is with the Centre for Quantum Computation and Intelligent Systems, Faculty of Engineering and Information Technology, University of Technology, Sydney 2007, Australia (e-mail: dacheng.tao@gmail.com).

Color versions of one or more of the figures in this paper are available online at http://ieeexplore.ieee.org.

Digital Object Identifier 10.1109/TGRS.2013.2245509

variation [10]–[12], texture synthesis [9], [13], and the Huber–Markov method [14], [15]. These algorithms are appropriate for the inpainting of small areas, but for large areas such as Aqua MODIS band 6, they are not so suitable. Happily, these deficiencies can be eliminated by virtue of the new compressed sensing (CS) theory. This indicates that a sparse signal under some transform domain or compressible signal can be approximately reconstructed from just a handful of incomplete information. Considering its powerful handling capacity, CS theory has come into use for remote sensing image processing, e.g., image fusion [16], [17], classification [18], [19], and unmixing [20], [21]. The CS and/or sparse image representation are then incorporated into image inpainting, in [22]–[24].

In this paper, we propose adaptive spectrum-weighted sparse Bayesian dictionary learning to effectively recover the Aqua MODIS band 6. In the CS framework, the latent spectral correlations between different spectral bands are utilized adaptively by the use of a beta process factor analysis (BPFA). The outcome is pleasing, on the premise of some mature image priors.

The rest of this paper is organized as follows. In Section II we survey the emerging and booming information sampling approach of CS theory; both the fertile image priors and the adaptive recovery model are discussed in succession. This is followed by the retrieval experiments in Section III, and the corresponding conclusions are summarized in Section IV.

II. RECOVERY METHOD

In the last decade, a great deal of effort has gone into the development of image inpainting. However, the majority of the recovery algorithms are focused on relatively ordinary or small-area information losing patterns, such as spots, stripes or random dead pixels. On the other hand, in view of the large-area periodic dead pixel phenomenon in the Aqua MODIS band 6, a few scholars have pioneered the reconstitution of the missing data based on the relationship between bands 6 and 7 (see [1], [2], [4]). However, the relationships between band 6 and the other bands are not exploited. This is until the recent birth of sparse representation and CS, both of which provide a possible approach to the previous problem. The former lays a solid theoretical foundation, and the latter solves many applied problems. Individually, Bayesian dictionary learning is a kind of sparse representation, which needs some proper prior image information. It happens that the spectral correlations can be employed by way of priors.

A. CS Theory

It is well-known that the traditional Nyquist–Shannon sampling theorem specifies that to avoid losing information when capturing a signal, one must sample at least two times faster than the signal bandwidth [25]. Nevertheless, the information we gain from the physical world is often abundantly redundant for many reasons. For example, the image data have many correlated forms, in general, and each form is often sensed by all kinds of sensors [26]. Is there any approach that could break through the bottleneck of recovery with only a few or incomplete measurements? Apparently, the answer is yes, and it is compressed/compressive sensing or compressed/compressive sampling that can settle this puzzle, as described by Donoho [27], Candes and Tao [28], and Romberg [29] in 2006. This method employs nonadaptive linear projections that preserve the structure of the signal; the signal is then reconstructed from these projections using an optimization process [25], setting off a revolution in signal processing.

In practice, CS aims to reconstruct a signal with incomplete and inaccurate measurements acquired by a projection matrix. Given a signal $x \in \mathbb{R}^N$ expressed as

$$x = \Psi\alpha \tag{1}$$

where $\Psi \in \mathbb{R}^{N\times N}$ is some orthogonal basis, and $\alpha \in \mathbb{R}^N$ is the basis coefficient. If α satisfies

$$\|\alpha\|_0 = K \ll N \tag{2}$$

where $\|\cdot\|_0$ is a zero norm, which means that the number of nonzero elements, x, can be called K-sparse to the basis Ψ. Then, on the condition of measurement matrix $\Phi \in \mathbb{R}^{M\times N}$ and $M < N$, there is a CS measurement $y \in \mathbb{R}^M$

$$y = \Phi x. \tag{3}$$

Substituting (1) for (3)

$$y = \Phi\Psi\alpha. \tag{4}$$

Equation (4) is the CS prototype, and by means of the sparse property, the ill-posed (4) can be solved by

$$\min \|\alpha\|_0 \ \text{ s.t. } \ y = \Phi\Psi\alpha. \tag{5}$$

Additionally, when $\Phi\Psi$ accords with a constraint factor called the restricted isometry property [29], (5) is equivalent to

$$\min \|\alpha\|_1 \ \text{ s.t. } \ y = \Phi\Psi\alpha \tag{6}$$

where $\|\cdot\|_1$ is the l_1 norm, implying the elements sum of absolute value for a vector. Until now, there are many reconstruction algorithms for CS, such as BP [30], OMP [31], ROMP [32], SP [33], CoSaMP [34], and so on.

B. Image Priors

CS indicates that a sparse signal under some transform domain or compressible signal can be approximately reconstructed from just a handful of incomplete information. Specifically, the transform domain amounts to a sparse basis, for which the course of looking is also cast as dictionary learning [26], [35]–[37]. The dictionary, of which the components are named atoms, is an overcomplete database, which can express the signal as a linear combination of a small number of atoms. In addition, dictionary learning has developed into a branch known as Bayesian dictionary learning [38]. Furthermore, it is recently considered as a factor analysis problem, with the factor loadings corresponding to the dictionary atoms [23]. Suppose an image $X \in \mathbb{R}^{m\times n\times b}$ consists of a series of partially overlapping patches $\{X_i \in \mathbb{R}^{m_1\times n_1\times b}\}_{i=1,\ldots,N}$ and is multi-spectral or hyperspectral, then the patches will be unwrapped into vectors

$\{x_i \in \mathbb{R}^P\}_{i=1,\ldots,N}$ and $P = m_1 \times n_1 \times b$, whereupon, the ith observation $y_i \in \mathbb{R}^P$

$$y_i = \Sigma_i \circ x_i \tag{7}$$

where the signature ($\circ$) is the point-wise product of the elements, and $\Sigma_i \in \mathbb{R}^P$ is the position matrix marking in which data needs recovering. Subsequently, the sparse representation of x_i is as follows:

$$x_i = D\alpha_i + \varepsilon_i \tag{8}$$

where $D \in \mathbb{R}^{P\times K}$ is the overcomplete dictionary [equal to the product of Φ and Ψ in (4)], with $\alpha_i \in \mathbb{R}^K$ signifying the coefficient of the dictionary, and $\varepsilon_i \in \mathbb{R}^P$ is the additive noise and model errors.

Priors are necessary in a Bayesian framework, and the beta-Bernoulli process provides a very convenient prior for the sparse coefficient, according to [23], [39], and [40]. This process, which refers to a combination of a beta distribution and a Bernoulli one, is just a pair of conjugate priors. The dictionary coefficient α_i is used instead of (9) to better exploit the sparsity

$$\alpha_i = z_i \circ s_i \tag{9}$$

where the sign ($\circ$) is the same as (7). $z_i \in \{0, 1\}^K$ is a binary vector implicating the K columns of D that are touched upon the presentation of x_i, and $s_i \in \mathbb{R}^K$ is the sparse coefficient, just like α_i, while z_i is absent. The concatenate model of (8) and (9) is the derivation of infinite sparse factor analysis [41], more detailed proofs are described in [41]. Conceptually, it is a nonparametric Bayesian extension of independent components analysis. Initially, the Gaussian prior is imposed on s_i as

$$s_i \sim N(0, \gamma_s^{-1} I_K) \tag{10}$$

where I_K is a $K \times K$ identity matrix, and γ_s is the hyperparameter obeying another hyperprior distribution

$$\gamma_s \sim \mathrm{Gamma}(a, b) \tag{11}$$

where a and b are the parameters of the Gamma distribution, and (10) and (11) are also a pair of conjugate priors which can be interpreted as a "distribution over distribution" [42].

Accordingly, α_i manifests more sparseness with z_i. z_i is a binary vector acting as a mask on s_i and further on D, which plays the part in specifying whether the hidden sources s_i and D are active in the corresponding position. Under this circumstance, the sparseness of the dictionary coefficients is manifested appropriately. Particularly, z_i is placed on the Bernoulli priors

$$z_i \sim \prod_{k=1}^{K} \mathrm{Bernoulli}(\pi_k) \tag{12}$$

where the notation Π does not denote the meaning of the product, as is the usual case, but every element of z_i, which has K elements in all, obeys a different Bernoulli distribution, and the argument π_k has a beta prior

$$\pi \sim \prod_{k=1}^{K} \mathrm{Beta}\left(\frac{c_0}{K}, \frac{d(K-1)}{K}\right) \tag{13}$$

where c_0 and d are the arguments of the beta distribution. The alliance of (12) and (13) is the above-mentioned beta-Bernoulli prior, as described in [23].

Similarly, D is imposed on some other prior by making its atoms d_k Gaussian distributed

$$d_k \sim N(0, P^{-1} I_P) \tag{14}$$

where $d_k \in \mathbb{R}^P$ is nothing but one column of the dictionary D, and I_P is a $P \times P$ identity matrix. In the process of dictionary learning, d_k is adaptively updated via Gibbs sampling according to the processing data itself [23]. The active sets are all drawn from the shared probability, which contributes to the encouraged consistent use of dictionary atoms. In addition, with the help of z_i, d_k could be used repeatedly for the representation of x_i, it is a very advantage when overlapped patches of images are processed.

The aforementioned image prior (14) can achieve good recovery effects to some extent; however, the spectral relationships between Aqua MODIS band 6 and the other bands are not taken advantage adequately. To remedy this imperfection, we propose an adaptive spectrum-weighted method. For this model, the prior of the dictionary is modified in accordance with (15), as follows:

$$d_k \sim N(0, (LPw)^{-1} I_P) \tag{15}$$

where L is a constant that is used to adjust the dictionary atom. It represents the joint correlation property of atoms that is a large deviation bound for sums of random variables [31]. To some extent, L can narrow the gaps of the elements of one atom so that the representation of the processed image approximates more to the ideal one. However, it does not allow for the latent band correlation. Therefore, w, a spectral weight which trades off the real correlation, is introduced. In this hierarchical system, the more correlated the two spectral bands are, the heavier the weight is. Nowadays, there are many indicators that can measure the relationship between two images, such as the correlation coefficient (CC), universal image quality index [43], and the structural similarity (SSIM) [44] index, and so on. Through a large number of trials over many granules of different types and seasons, the SSIM index evaluates the spectral correlation most accurately in our inpainting case. That is, the spectral complementarity and correlation are considered via the band weight of the SSIM index.

SSIM is a kind of similarity measurement, proposed by Zhou [44] in 2004, and is composed of three independent comparisons of luminance, contrast, and structure, as

$$S(x, y) = f(l(x, y), c(x, y), s(x, y)) \tag{16}$$

where x and y are two nonnegative image signals, and $S(x, y)$, $l(x, y)$, $c(x, y)$, and $s(x, y)$ are the SSIM index, luminance, contrast, and structure function of the two signals, respectively. For the luminance function

$$l(x, y) = \frac{2\mu_x\mu_y + C_1}{\mu_x^2 + \mu_y^2 + C_1} \tag{17}$$

where μ_x is the mean intensity of x, μ_y is the mean intensity of y, and C_1 is just a constant. Moreover, as far as the second comparison contrast is concerned, it has a similar modality to (17), and the definition is

$$c(x, y) = \frac{2\sigma_x\sigma_y + C_2}{\sigma_x^2 + \sigma_y^2 + C_2} \tag{18}$$

where σ_x and σ_y are the standard deviation of the image signals x and y, and C_2 is another constant. Here, the structure function is as follows:

$$s(x, y) = \frac{\sigma_{xy} + C_3}{\sigma_x\sigma_y + C_3} \tag{19}$$

where C_3 is also a constant, and σ_{xy} is the covariance of x and y.

Finally, a combination of the three functions can be described as another abstract form

$$S(x, y) = [l(x, y)]^\alpha \cdot [c(x, y)]^\beta \cdot [s(x, y)]^\gamma. \tag{20}$$

α, β, and γ (all positive numbers) are applied to coordinate the relative importance of the three compositions. When $\alpha = \beta = \gamma = 1$ and $C_3 = C_2/2$, finally, (20) can be substituted by

$$S(x, y) = \frac{(2\mu_x\mu_y + C_1)(2\sigma_{xy} + C_2)}{(\mu_x^2 + \mu_y^2 + C_1)(\sigma_x^2 + \sigma_y^2 + C_2)}. \tag{21}$$

Even if the SSIM is a measure that encodes some heuristic characteristics of the human visual system to produce a quantitative measure of perceptual similarity, it can also be thought of as a similarity measure for comparing any two signals, because of its symmetry measure [44]. It consists of three independent components (luminance, contrast and structure) that measure the similarities from three different aspects. In other words, this similarity measure can also be considered as a measure of the spectral structure correlation. Hence, the SSIM is taken as a spectrally similar weight integrated into the adaptive recovery model.

In (15), w is a diagonal matrix, of which the elements are the SSIM of band 6 and the other bands as

$$w_{ii} = S_i \tag{22}$$

where S_i is the SSIM index of bands i and 6, and w_{ii} is the diagonal element.

Actually, in Aqua/Terra MODIS L1B products, they all have only seven bands, which sense the earth's surface with different wavelengths of 0.620–0.670, 0.841–0.876, 0.459–0.479, 0.545–0.565, 1.230–1.250, 1.628–1.652, and 2.105–2.155 μm, resulting in the reflectance shifting significantly. Just as its name implies, SSIM measures the similarity of two given images from the viewpoint of structure. To weaken the influence of luminance so that the similarities of band 6 and the other bands are measured more accurately, we undertook image normalization before SSIM is calculated. In the field of image processing, there are lots of ways of normalizing, and we chose a plain and fundamental one: the pixel values except those of band 6 are added or subtracted by the mean value difference with band 6.

Finally, an analogical prior to s_i is appended to the noise and model errors ε_i

$$\varepsilon_i \sim N(0, \gamma_\varepsilon^{-1} I_P). \tag{23}$$

Here, I_P is identical to that in (14). In addition, the prior of γ_ε has a parallel counterpart of γ_s

$$\gamma_\varepsilon \sim \text{Gamma}(e, f). \tag{24}$$

C. Adaptive Recovery Model

A significant advantage with the ample hierarchical prior distributions above is that the posterior update equation in the Bayesian system is analytical. However, (14) hardly makes use of the complementary spectral relations, so a new paradigm (15) is drawn into by the weight of the SSIM index.

To generalize the above formulae, a hierarchical model is introduced: adaptive BPFA (ABPFA), as shown in

$$\begin{aligned} y_i &= \Sigma_i \circ x_i \\ x_i &= D\alpha_i + \varepsilon_i \\ \alpha_i &= z_i \circ s_i \\ s_i &\sim N(0, \gamma_s^{-1} I_K) \\ d_k &\sim N(0, (LPw)^{-1} I_P) \\ \varepsilon_i &\sim N(0, \gamma_\varepsilon^{-1} I_P). \end{aligned} \tag{25}$$

Overall, if d_k obeys a distribution as (14), substituting for the counterpart in (25), this model (the others remain the same) is the primitive BFPA [23] model. Under such a framework, the inference and solution of this process are implemented via Gibbs sampling, as described in [23]. The Gaussian priors for d_k and s_i can provide the model convenience with consecutive conjugacy in the hierarchical model. The dictionary learning mode known as online dictionary learning [37], [45] can learn a redundant dictionary in situ, in which a library of training images is not necessary, based on the offline mode.

III. RECOVERY EXPERIMENTS

For the purpose of intuitive illustration, we conduct both simulated and real experiments. The proposed restoring algorithm can be used on both 500- and 1000-m resolution; for brevity, we just applied it to 500-m images. Initially, we describe the simulation experiments by the metrics of SSIM, CC, and peak signal to noise ratio (PSNR), followed by an analysis of the multifarious factors affecting the recovery precision. Secondly, the real recovery of Aqua MODIS band 6 is evaluated with the objective metric of noise reduction (NR). The Aqua/Terra MODIS image data used in the following experiments are the reflectance (between zero and one), and are not georectified. They are cropped from the granules that are downloaded from the NASA L1B product website (http://ladsweb.nascom.nasa.gov/data/search.html). As is well-known, for Terra and Aqua MODIS, there are some bands contaminated by striping noise, such as bands 3, 5, and 7 of Terra MODIS; fortunately, the type of striping noise is not complicated. In view of this situation, to mitigate some of the effects on the proposed method resulting from the stripes, we removed them by the simple average of the upper and lower lines of the stripe line.

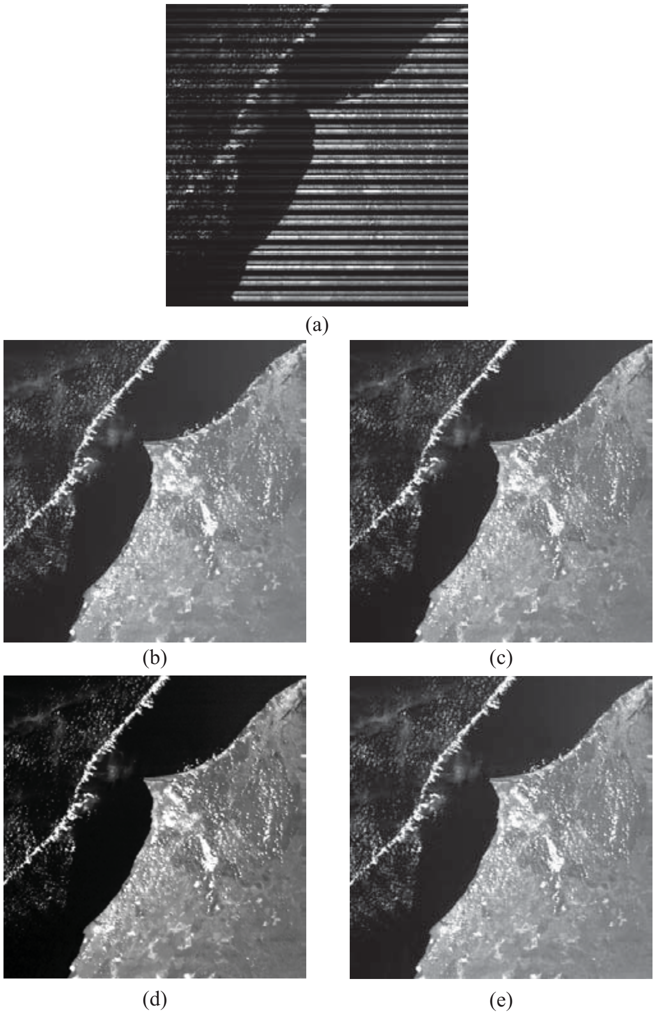

Fig. 1. Simulated Terra recoveries (acquired on August 1, 2009), with size of 400 × 400 × 7. (a) Simulated corruption of Terra MODIS band 6. (b) HMLLSF recovery. (c) WCLF recovery. (d) BPFA recovery. (e) ABPFA recovery.

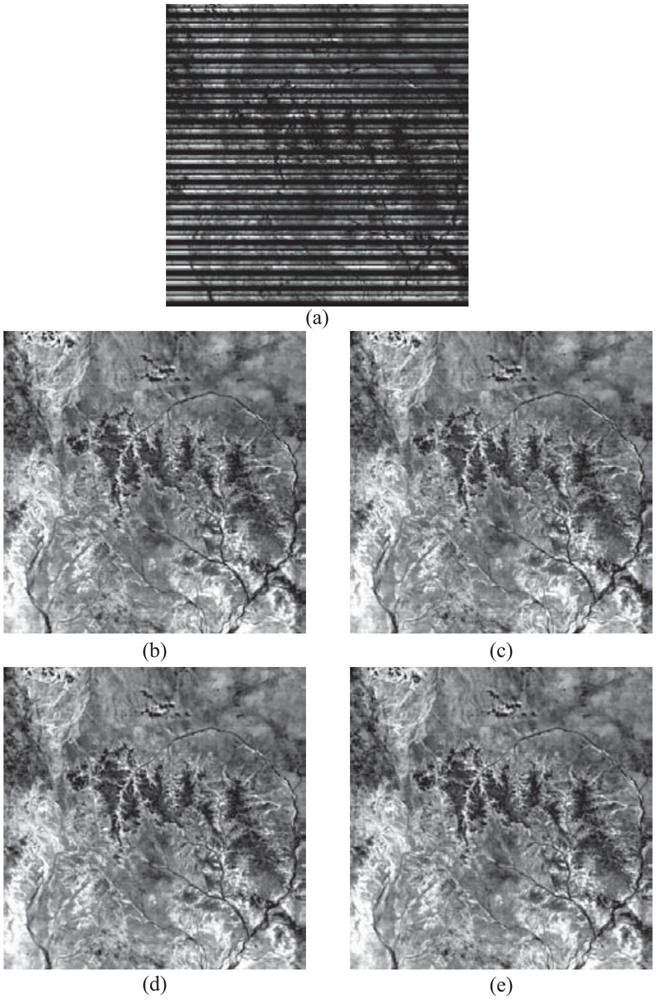

Fig. 2. Simulated Terra recoveries (acquired on April 1, 2003), with size of 400 × 400 × 7. (a) Simulated corruption of Terra MODIS band 6. (b) HMLLSF recovery. (c) WCLF recovery. (d) BPFA recovery. (e) ABPFA recovery.

A. Simulation Recovery Experiments

To allow a quantitative evaluation, we first undertook some simulated recovery experiments. Generally, the Terra MODIS and Aqua MODIS have analogous design patterns, which make it possible to evaluate the retrieval method by simulating the damage to Aqua MODIS band 6 on Terra MODIS band 6. In our experiments, the degradation of Aqua MODIS band 6 is simulated using the twin Terra MODIS band 6 that does not have the nonfunctioning problem. To test the effectiveness of the proposed model, we undertook two simulation experiments with images acquired on August 1, 2009 (Fig. 1), and on April 1, 2003 (Fig. 2), respectively, with a subregion of 400 × 400 × 7. The simulated corrupt images of band 6 are shown in Figs. 1(a) and 2(a). In these two experiments, the size of the overlapping image patches is 4 × 4 × 7 (the L1B product of MODIS has seven spectral bands, and the nadir spatial resolution in all bands is 500 m), so $P = 112$. K is set to 256 as usual. Therefore, D is a matrix of 112 × 256. The other parameters are $a = b = e = f = 1 \times 10^{-6}$, $c_0 = d = 1$, $L = 80$, $C_1 = 1 \times 10^{-4}$, and $C_2 = 9 \times 10^{-4}$. Figs. 1 and 2 show the simulated corruptions and the corresponding recoveries by the histogram matching and local least squares fitting (HMLLSF) [1], WCLF [4], and BPFA [23] methods. However, from the subjective point of view of a visual assessment, the recovery differences cannot be determined, and let alone their advantages and disadvantages.

Therefore, objective quantitative contrasts for the four methods are made with regard to SSIM, CC, and PSNR. Initially, the CC of signals/images x and y is calculated by the following:

$$\mathrm{CC}(x,\, y) = \frac{\sum_{i=1}^{N}(x_i - \mu_x)(y_i - \mu_y)}{\sqrt{\sum_{i=1}^{N}(x_i - \mu_x)^2}\sqrt{\sum_{i=1}^{N}(y_i - \mu_y)^2}} \tag{26}$$

where μ_x and μ_y are the matching mean values.

The PSNR is most commonly used as the measure of the quality of the reconstruction of lossy codecs. Generally, the higher it is, the better the quality is. For a double-precision image, which has pixel values between zero and one, the PSNR is calculated by

$$\mathrm{PSNR}(x,\, y) = -10 \log_{10}\left(\frac{1}{N}\sum_{i=1}^{N}(x_i - y_i)^2\right). \tag{27}$$

TABLE I
RECOVERY RESULTS OF TERRA MODIS BAND 6
BY DIFFERENT METHODS

Images	Methods	SSIM	CC	PSNR/dB
Fig. 1	HMLLSF	0.98076	0.99281	41.0822
	WCLF	0.98221	0.99304	41.1712
	BPFA	0.98444	0.99529	42.8943
	ABPFA	**0.98905**	**0.99619**	**43.7922**
Fig. 2	HMLLSF	0.98403	0.98248	42.7871
	WCLF	0.98491	0.98539	43.4987
	BPFA	0.99014	0.98895	44.8417
	ABPFA	**0.99170**	**0.99065**	**45.5613**

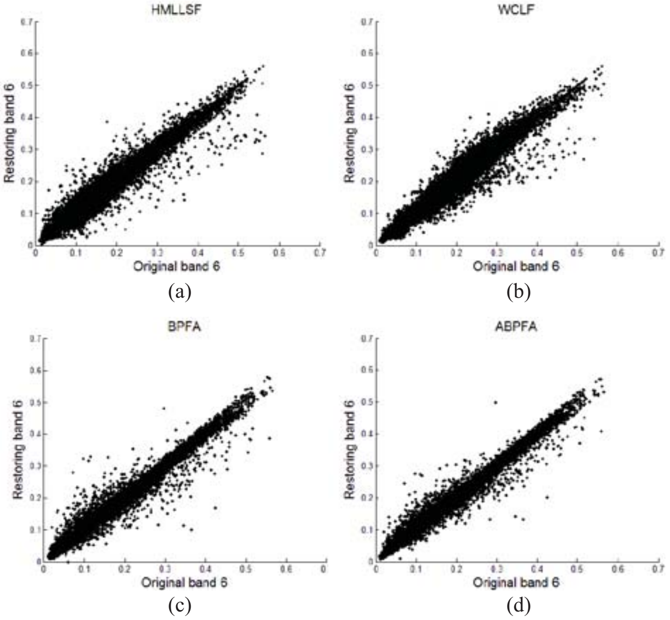

(a) (b)
(c) (d)

Fig. 3. Scatter plots between simulated and recovered Terra MODIS band 6 in Fig. 1. (a) HMLLSF method. (b) WCLF method. (c) BPFA method. (d) ABPFA method.

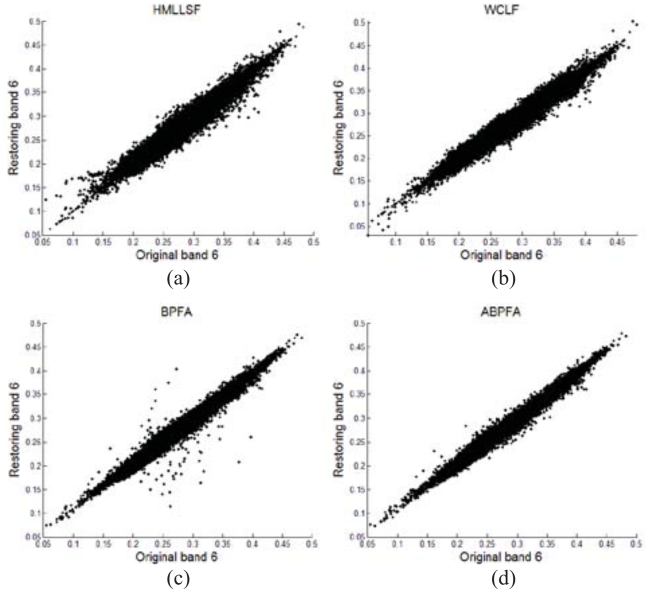

(a) (b)
(c) (d)

Fig. 4. Scatter plots between simulated and recovered Terra MODIS band 6 in Fig. 2. (a) HMLLSF method. (b) WCLF method. (c) BPFA method. (d) ABPFA method.

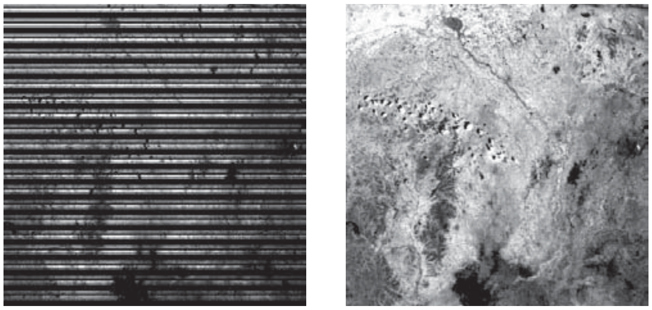
(a) (b)

Fig. 5. Simulated Terra recoveries (acquired on May 8, 2008), with size of 400 × 400 × 7. (a) Simulated corruption of Terra MODIS band 6. (b) ABPFA recovery.

The SSIM, CC, and PSNR values between the Terra MODIS intact band 6 and the recovered images [Figs. 1(b)–(e) and 2(b)–(e)] are shown in Table I. Compared with the HMLLSF, WCLF, and BPFA methods, the SSIM, CC, and PSNR values of the proposed ABPFA method are all clearly improved. In addition, as far as these evaluation targets go, BPFA is better than HMLLSF and WCLF. This is because the HMLLSF and WCLF algorithms exploit the relation of bands 6 and 7 alone, but BPFA utilizes the spectral relations between band 6 and all the other bands. However, the spectral weights are parallel in the BPFA framework structure, in which the actual relationships are ignored. Given this imperfection, ABPFA weighs the spectral correlations adaptively, relying on their practical significance; therefore, it has the best recovery result. As a whole, a rough ranking of the inpainting effects, from worst to best, is as follows: HMLLSF, WCLF, BPFA, and ABPFA.

To make a more straightforward comparison with these aforementioned methods, we drew some scatter diagrams. Fig. 3(a)–(d) shows the scatter plots between the original and recovered images for Fig. 1(a), using the HMLLSF, WCLF, BPFA, and ABPFA methods, respectively. Generally, the points of HMLLSF and WCLF scatter most discretely, accompanied with many false outliers; those of BPFA become thinner with less discrete points; and ABPFA is the best method accordingly. The commensurate counterparts for Fig. 2(a) are shown in Fig. 4. In general, the scatter plots in Figs. 3 and 4 agree with the quantitative evaluation in Table I.

Here, to ensure a comprehensive assessment of the proposed algorithm, we undertook another two similar simulation experiments. The Terra MODIS images were acquired on May 8, 2008, and January 1, 2008, respectively, as shown in Figs. 5 and 6. Identical parameters to those used in the last experiment are used. From a visual perspective, the band 6 images are perfectly recovered. The quantitative evaluations of the previous methods are shown in Table II, and it is not difficult to arrive at the pleasing conclusion that both Tables I and II confirm that the proposed method outperforms all the other methods.

We describe the verification experiments undertaken on the factors making a difference to the accuracy of the proposed ABPFA method, accompanied with an analysis and discussion.

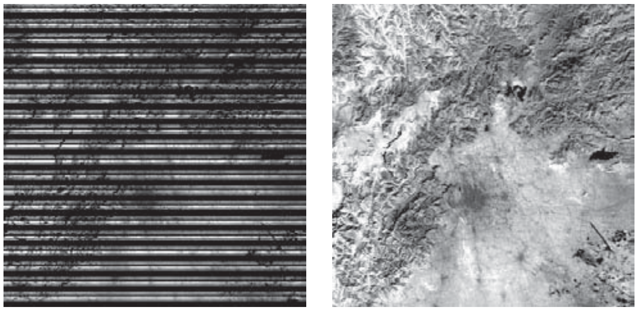

(a) (b)

Fig. 6. Simulated Terra recoveries (acquired on January 1, 2008), with size of 400 × 400 × 7. (a) Simulated corruption of Terra MODIS band 6. (b) ABPFA recovery.

TABLE II
RECOVERY RESULTS OF TERRA MODIS BAND 6

Images	Methods	SSIM	CC	PSNR/dB
Fig. 5	HMLLSF	0.98634	0.99560	44.0449
	WCLF	0.98658	0.99623	44.6419
	BPFA	0.98873	0.99678	45.4552
	ABPFA	**0.99071**	**0.99733**	**46.2218**
Fig. 6	HMLLSF	0.98601	0.97502	45.8223
	WCLF	0.98818	0.98455	47.8810
	BPFA	0.99027	0.98595	48.2368
	ABPFA	**0.99083**	**0.98740**	**48.6356**

TABLE III
RECOVERY RESULTS FOR VALIDATION OF INFLUENCE OF SSIM BEING CALCULATED BEFORE AND AFTER IMAGE NORMALIZATION

Images	Normalization	SSIM	CC	PSNR/dB
Fig. 1	No	0.98744	0.99578	43.3447
	Yes	**0.98905**	**0.99619**	**43.7922**
Fig. 2	No	0.99113	0.99008	45.2888
	Yes	**0.99170**	**0.99065**	**45.5613**

It is declared in Section II-C that image normalization is of great significance before SSIM is calculated. The following verification experiment is performed for Figs. 1(a) and 2(a) to test this assumption. In this experiment, all the settings are the same, except for the calculation of SSIM. The recovery results of the two images by ABPFA with SSIM calculated, before and after image normalization, are shown in Table III. The results are better when the SSIMs of band 6 and the other bands are calculated after image normalization. Because the reflectance of the seven bands varies widely in intensity, and SSIM has a close relationship with the intensity, if the images are not normalized when SSIM is calculated, the band similarities (mainly referring to the similarities in the image structure) are measured less precisely. After normalization, the discrepancies in the intensity of all seven bands will be weakened, so the similarities in the structure can be strengthened accordingly. Ultimately, this way of calculating SSIM estimates the weights of band similarity more precisely. It is important that the normalization is just used for the calculation of SSIM, not for the image retrieval.

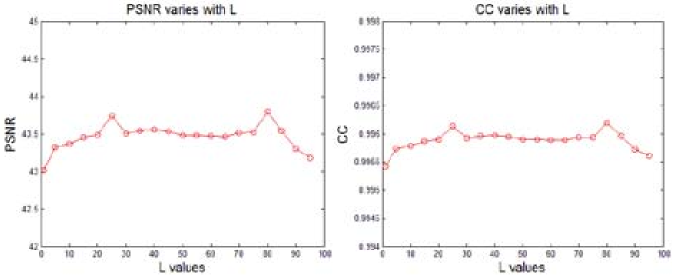

(a) (b)

Fig. 7. PSNR and CC vary with different L parameters for Fig. 1 (by ABPFA). (a) PSNR varies with L. (b) CC varies with L.

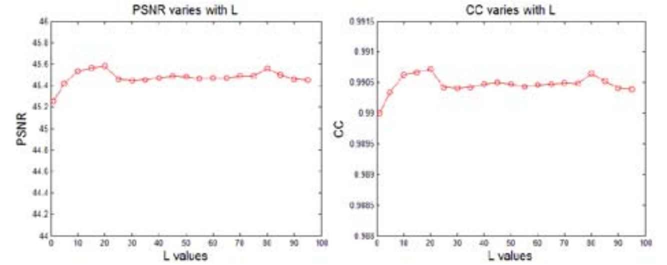

(a) (b)

Fig. 8. PSNR and CC vary with different L parameters for Fig. 2 (by ABPFA). (a) PSNR varies with L. (b) CC varies with L.

The contributions that the different bands made to the recovery of band 6 are revealed by the recovery experiments of Figs. 1(a) and 2(a). Table IV shows the recovery results with another two bands, using the BPFA and ABPFA methods, except for the last column, which uses all seven bands. The SSIM, CC, and PSNR values between the intact and recovered band 6 are taken as the evaluation indicators. In this table, "Bands" represents the bands that are utilized to recover band 6. Whether using BPFA or ABPFA, the differences in the recoveries with the different bands are all obvious. The Terra/Aqua MODIS band 6 has a different correlation with the other bands, such as the visible, near-IR, and middle-IR, which brings about a direct influence on the recovery effects. Generally, bands 2, 5, and 7 are more similar than the other bands in the L1B product, so better results are obtained when using them, no matter whether BPFA or ABPFA is used. Therefore, it is important to take the different functions of the different bands into account. In addition, the outcome of the recovery using only two bands is not as good as that using seven bands, because of the reduced amount of available information.

In (15), L and $\mathbf{w}$ are both introduced for the remarkably important role that they play in the recovery. The importance of these parameters is investigated in a further verification experiment. In Table V, we list the recovery results of the different ways of weighing the band similarities between band 6 and the other bands for Figs. 1(a) and 2(a), and their corresponding counterparts multiplied by parameter L (e.g., 10). To save time, we used 2 × 2 × 7 image patches here. In the framework of ABPFA, BPFA amounts to the situation where the value of L is one and $\mathbf{w}$ has all ones (equivalent weights). L plays an important part in the adjustment of the joint correlation of the dictionary atoms and $\mathbf{w}$ measures the

TABLE IV

RECOVERY RESULTS FOR VALIDATION OF BAND CONTRIBUTIONS RECOVERED TERRA MODIS BAND 6 BY ANOTHER TWO DIFFERENT BANDS

Images	Methods	Bands	(3, 4, 6)	(2, 3, 6)	(1, 2, 6)	(4, 5, 6)	(2, 6, 7)	(5, 6, 7)	All
Fig. 1	BPFA	CC	0.88984	0.93936	0.96615	0.97444	0.98850	0.99081	0.99529
	ABPFA		**0.90440**	**0.95336**	**0.97016**	**0.97564**	**0.98895**	**0.99146**	**0.99619**
	BPFA	PSNR/dB	28.6457	31.8853	34.3196	35.5218	38.7452	39.9489	42.8943
	ABPFA		**29.3722**	**33.0185**	**34.8076**	**35.6851**	**38.9085**	**40.2509**	**43.7922**
	BPFA	SSIM	0.87766	0.91808	0.94143	0.94686	0.96184	0.96825	0.98444
	ABPFA		**0.89371**	**0.92981**	**0.94541**	**0.94856**	**0.96274**	**0.97059**	**0.98905**
Fig. 2	BPFA	CC	0.79790	0.84611	0.90392	0.93053	0.94696	0.96198	0.98895
	ABPFA		**0.82589**	**0.84969**	**0.90663**	**0.93341**	**0.94848**	**0.96545**	**0.99065**
	BPFA	PSNR/dB	32.7141	33.7934	35.3074	37.0372	37.5674	39.3397	44.8417
	ABPFA		**33.3182**	**33.8926**	**35.4428**	**37.2114**	**37.6934**	**39.7098**	**45.5613**
	BPFA	SSIM	0.91927	0.92280	0.93886	0.94902	0.95359	0.96147	0.99014
	ABPFA		**0.92113**	**0.92752**	**0.93887**	**0.95237**	**0.95547**	**0.96666**	**0.99170**

TABLE V

RECOVERY RESULTS FOR VALIDATION OF INFLUENCES OF L AND w

Images	Methods	L	**w**	SSIM	CC	PSNR/dB
Fig. 1	BPFA	1	**1**	0.97302	0.99196	40.5931
	ABPFA (CC)	1	CC	0.97342	0.99204	40.6360
	ABPFA (SSIM)	1	SSIM	**0.97483**	**0.99254**	**40.9161**
	BPFA (×10)	10	**1**	0.98350	0.99513	42.7475
	ABPFA (CC ×10)	10	CC	0.98384	0.99527	42.8727
	ABPFA (SSIM ×10)	10	SSIM	**0.98511**	**0.99557**	**43.1549**
Fig. 2	BPFA	1	**1**	0.98186	0.98223	42.7839
	ABPFA (CC)	1	CC	0.98205	0.98270	42.9007
	ABPFA (SSIM)	1	SSIM	**0.98226**	**0.98321**	**43.0472**
	BPFA (×10)	10	**1**	0.99019	0.98954	45.0676
	ABPFA (CC ×10)	10	CC	0.99023	0.98973	45.1533
	ABPFA (SSIM ×10)	10	SSIM	**0.99074**	**0.98987**	**45.2009**

L and $\mathbf{w}$: the parameters in (25).

latent band similarity. The table shows that, for the same method with identical $\mathbf{w}$, but with different L (one or ten), the results with L being ten become much better. This is because when L has the value of ten, the joint atom correlation is more suitable, which contributes to the image representation being closer to the perfect situation. Additionally, it also shows that no matter whether $L = 1$ or 10, on the premise that L has the same value, the recovery effect becomes better according to the order of BPFA, ABPFA (CC), and ABPFA (SSIM). This illustrates that SSIM weighs the band similarity more precisely than CC. Here, we just take SSIM as a relative weight to measure the band similarity between band 6 and the other bands. It is more important that the result is encouraging. In terms of the reflectance used in our experiments, we set SSIM as a relative indicator, not an absolute one, trading off the actual importance, so it does not settle out the physical terms from the perceptual terms.

Figs. 7 and 8 show the PSNR and CC values between the image recovered (by ABPFA) and the original band 6 images (for Figs. 1 and 2, respectively) varying with different values of the parameter L [see (15)]. In both Figs. 7 and 8, L ranges from 5 to 95, with an increment of five, except for the initial value one, which is equivalent to the occasion in which there is no L in (15). Broadly speaking, Fig. 8(a) and (b) have the same variation tendency; two small peaks at the horizontal ordinates of 20 and 80, and a minimum at the horizontal ordinate of one. Analytically, from previous section, L plays an important role in the joint correlation of the dictionary atoms. When $L = 1$, it does not affect the correlation, so the recovery outcome is the worst. In contrast, when it works, the result becomes better. In addition, if L is larger than ten and increases in a certain range, its capability of adjusting the correlation is strong, and changes little, as shown in Figs. 7 and 8. After a great number of tests, we discovered that L is connected to the information loss type of the diverse sensor types. In other words, the different types of information loss hold different values of L when the joint correlation is optimally considered. Generally, for Aqua MODIS band 6, the correlation is optimal whereas L has a value of between 20 and 80.

As with most other image block processing methods, the inpainting result by ABPFA is affected by the patch size. In Figs. 1 and 2, we only chose one popular kind of patch size at $4 \times 4 \times 7$. In general, the program takes a multiple of the running time as the proportionate relation of the patch size. Overall, we adopted $4 \times 4 \times 7$ patches in all the experiments, except in Tables V and VI, in which the objective is to validate the influence of the different patch sizes on the result of the inpainting. Similarly, in Table VI (Fig. 9), we took pending

TABLE VI
RECOVERY RESULTS OF DIFFERENT IMAGE PATCH SIZES

Images	Patches	$2 \times 2 \times 7$	$3 \times 3 \times 7$	$4 \times 4 \times 7$	$5 \times 5 \times 7$	$6 \times 6 \times 7$	$7 \times 7 \times 7$	$8 \times 8 \times 7$
Fig. 9(a)	SSIM	0.98278	0.98931	0.99418	**0.99423**	0.99405	0.99379	0.99333
	CC	0.98536	0.99221	0.99688	**0.99710**	0.99701	0.99689	0.99662
	PSNR/dB	40.5457	43.3099	47.2768	**47.5929**	47.4651	47.2924	46.9312
Fig. 9(c)	SSIM	0.99195	**0.99233**	0.99212	0.99183	0.99102	0.99034	0.98887
	CC	0.99099	0.99151	**0.99206**	0.99180	0.99144	0.99088	0.98994
	PSNR/dB	46.1907	46.4702	**46.7614**	46.6490	46.4479	46.1666	45.7330
Fig. 9(e)	SSIM	0.98409	**0.98440**	0.98230	0.97927	0.97668	0.97443	0.97086
	CC	0.98743	0.98981	**0.99002**	0.98875	0.98751	0.98722	0.98488
	PSNR/dB	41.7321	42.6592	**42.7649**	42.2533	41.8165	41.7234	40.9937
Fig. 9(g)	SSIM	0.98004	0.98053	**0.98063**	0.97891	0.97826	0.97671	0.97466
	CC	0.97923	0.97977	**0.97996**	0.97786	0.97710	0.97522	0.97225
	PSNR/dB	43.4530	43.5535	**43.5904**	43.1704	43.0497	42.7209	42.2366

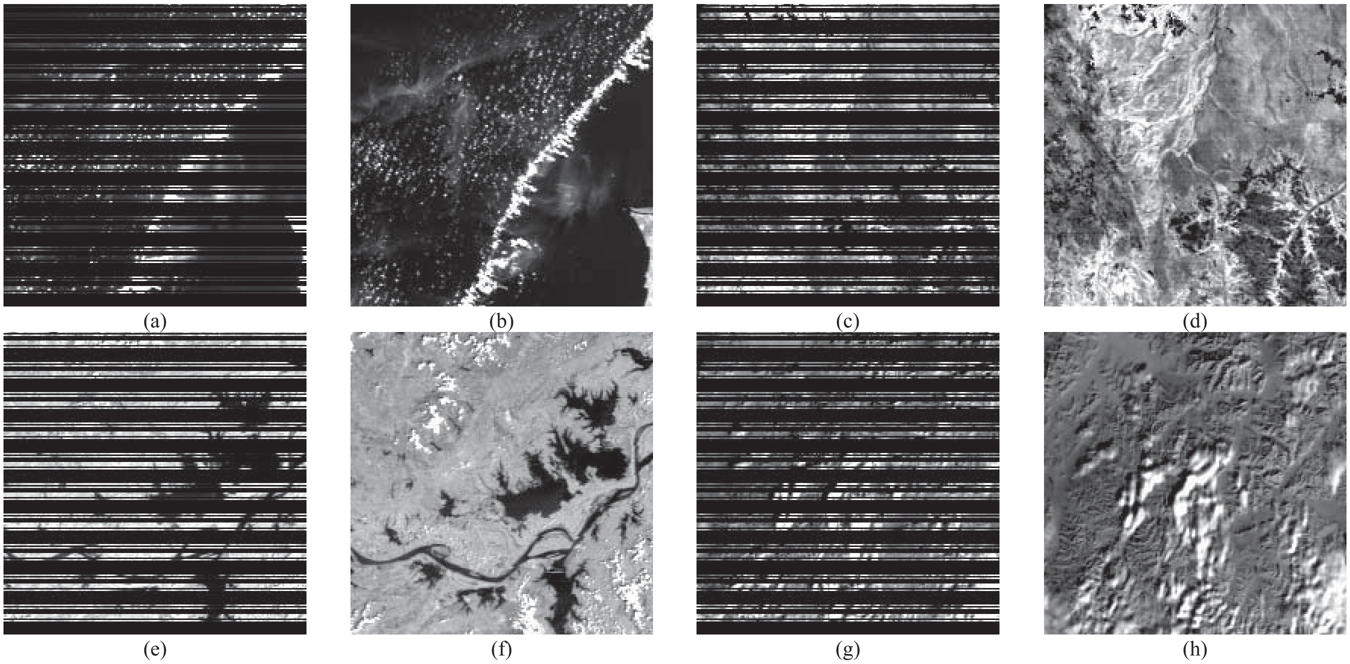

Fig. 9. Recovery results of four Terra MODIS band 6 images by ABPFA. Images are all $200 \times 200 \times 7$. (a), (c), (e), and (g) are simulated corruption of four images and (b), (d), (f), and (h) are their matching recoveries, respectively.

images with a size of $200 \times 200 \times 7$ to save time, with the patch sizes ranging from $2 \times 2 \times 7$ to $8 \times 8 \times 7$. In addition, the four images have manifold types of feature distribution, and the discrepancies are great in both their textures and gray ranges. From the impersonal metric indicators of SSIM, CC, and PSNR in Table VI, the patch should not be undersized or oversized. Therefore, on the one hand, if it is too small, the structural information and spatial correlation are easily overlooked. On the other hand, redundant information is introduced by the overlapping blocks with large patch sizes. For example, the latent relationship is undermined with an oversized, man-made and segmented neighborhood of image objects. In Table VI, the recovery results of Fig. 9(a), (c), (e), and (g) show that the medium sizes of $4\times4\times7$ or $5\times5\times7$ give first-class effects. In a nutshell, for most of the Terra MODIS images, the $4 \times 4 \times 7$ patches result in the best recoveries [e.g., Fig. 9(c), (e), and (g)]. Nonetheless, Fig. 9(a) does not conform to this rule, with the reason being that its dynamic range of gray is plain, that is, the pixels are either white or black (without smooth transition). Accordingly, the optimal patch size becomes larger ($5 \times 5 \times 7$). However, the results of the $4 \times 4 \times 7$ and $5 \times 5 \times 7$ patches are only just differentiable.

B. Recovery of Real Aqua MODIS Band 6

In this experiment, real images of Aqua MODIS band 6 are used, shown in Fig. 10(a) (acquired on January 18, 2009) and Fig. 11(a) (acquired on September 1, 2008). The size of the Aqua MODIS images is $400 \times 400 \times 7$ (cropped). The SSIM indexes are calculated by the region of the five detectors (a 25% in total, the same as the simulated experiments) that are working well. The other parameters in the ABPFA approach are the same as in the foregoing simulation recovery experiments for Terra. Figs. 10 and 11 show the recovery

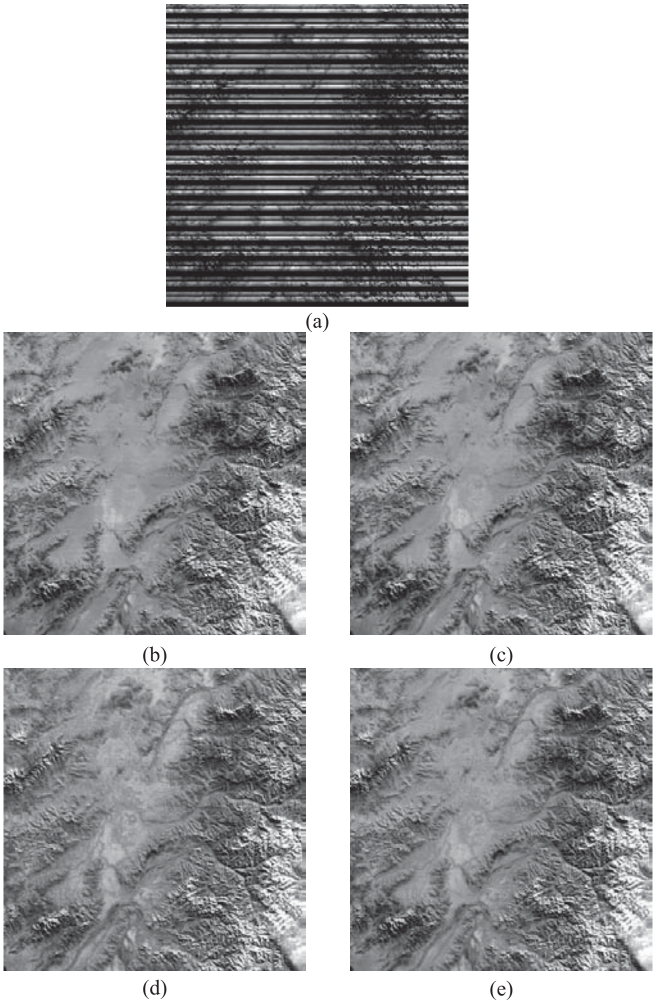

(a)

(b) (c)

(d) (e)

Fig. 10. Aqua recoveries (acquired on January 18, 2009), with size of 400 × 400 × 7. (a) Original Aqua MODIS band 6. (b) HMLLSF recovery. (c) WCLF recovery. (d) BPFA recovery. (e) ABPFA recovery.

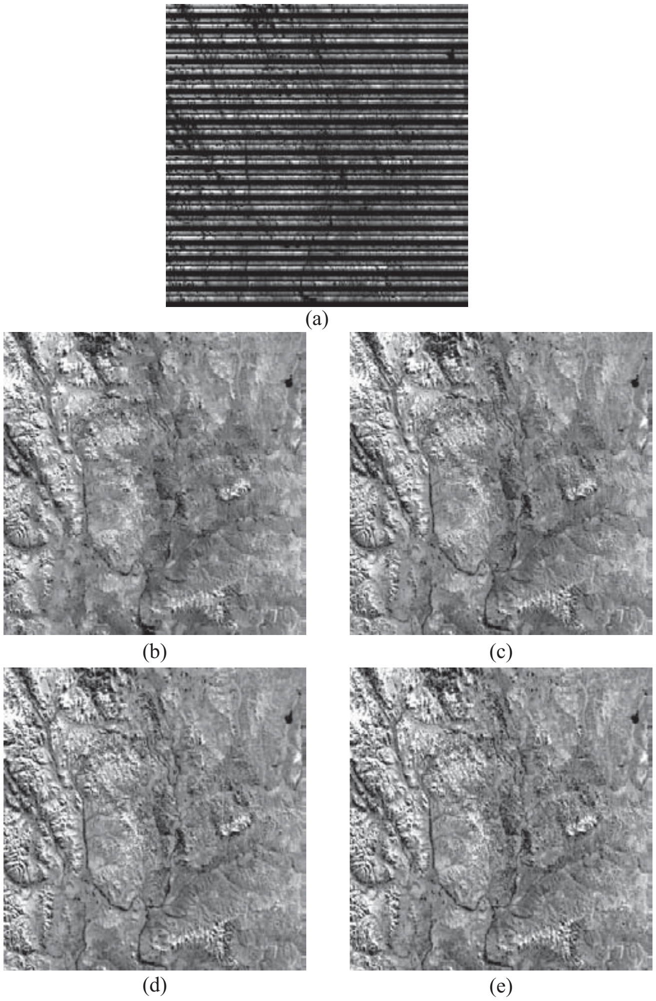

(a)

(b) (c)

(d) (e)

Fig. 11. Aqua recoveries (acquired on September 1, 2008), with size of 400 × 400 × 7. (a) Original Aqua MODIS band 6. (b) HMLLSF recovery. (c) WCLF recovery. (d) BPFA recovery. (e) ABPFA recovery.

TABLE VII

NR RATIOS OF ORIGINAL AND RECOVERED AQUA MODIS BAND 6 DATA

Images	Original	HMLLSF	WCLF	BPFA	ABPFA
Fig. 10	1.0000	122.2345	120.9718	126.3384	**128.5941**
Fig. 11	1.0000	912.1388	784.7355	883.5137	**1006.6000**

results of the two different Aqua MODIS band 6 images by the different methods.

Based on the two real experiments, in both Figs. 10 and 11, in terms of a visual judgment, the reconstruction results of HMLLSF and WCLF are closer to that of ABPFA. The reason is that HMLLSF and WCLF are based on the relation of bands 6 and 7, but BPFA draws support from the equally spectral weights of all bands, and ABPFA adaptively sets the weights depending on their real relative importance. It is important that, in the framework of ABPFA, the weight of band 7 is the largest (some researchers have confirmed that the radiative properties of bands 6 and 7 are very similar, as described in [1], [2], and [4]); although HMLLSF and WCLF only use the correlation between the two bands, it actually increases the weight of band 7 to some degree, which is very similar to ABPFA. Ultimately, the visual effects of HMLLSF, WCLF, and ABPFA are approximately equal to each other. It is this point that is neglected by the BPFA results in some dissimilarities. More intuitively, the inconsistency of HMLLSF and WCLF acts on our visual subjective feelings, to a greater or lesser degree.

Because of the lack of primary intact image data, the assessment criteria used in the simulation experiments are not applicable to the real experiments, so we resorted to evaluating the recovered images in the frequency domain by the ratio of NR [4]. The higher the NR is, the more the noise is reduced. It has the following definition:

$$\mathrm{NR} = \frac{N_0}{N_1} \tag{28}$$

where N_0 is the power of the frequency ingredients provided by the dead pixel stripes in the original image and N_1 is the retrieved image.

The corresponding NR values for Figs. 10 and 11 are shown in Table VII. Table VII shows that the values of NR for Fig. 11 by the four methods are greater than those of Fig. 10, with the reason for this being that the other spectral bands are

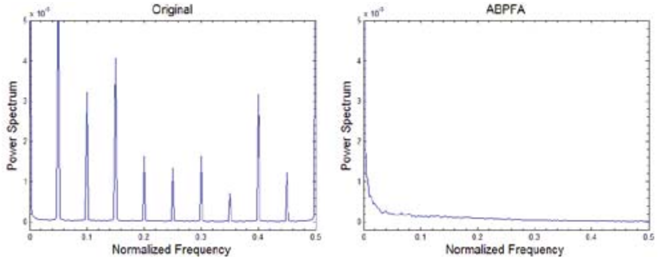

(a) (b)

Fig. 12. Mean column power spectrum of original Aqua MODIS band 6 and ABPFA recovery in Fig. 10. (a) Original. (b) ABPFA recovery.

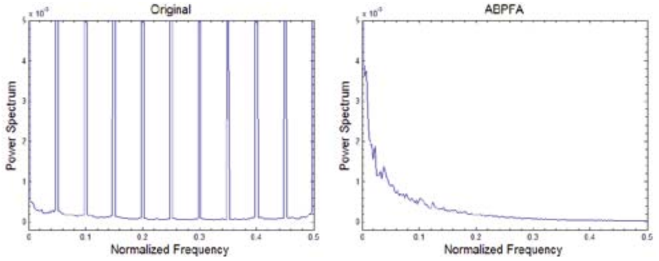

(a) (b)

Fig. 13. Mean column power spectrum of original Aqua MODIS band 6 and ABPFA recovery in Fig. 11. (a) Original. (b) ABPFA recovery.

more correlated with band 6 in Fig. 11. Unlike the simulated experiments, the HMLLSF method obtains better evaluation results than the WCLF and BPFA methods in terms of the NR index. The reason for this is that HMLLSF employs histogram matching, which contributes to improving the NR values, as described in [1]. In spite of this, the proposed ABPFA still results in the highest NR, meaning the most NR, which owes much to the weight of the band similarities involved in the handling process.

Figs. 12 and 13 show the Fourier transforms of the original and inpainted Aqua MODIS data (for Figs. 10 and 11 respectively). The dead pixel stripes are displayed in the frequency domain. Fortunately, the proposed ABPFA can effectively remove the frequency pulses caused by the dead pixel stripes. The results are both fascinating and smoother.

With a subjective evaluation, many different approaches to the recovery of Aqua MODIS band 6 achieved appealing results (e.g., WCLF, HMLLSF). However, with an objective quality metric perspective, this is often not the case as the latent spectral relations are not being made the most of. It is this point that is settled by the proposed adaptive spectrum-weighted sparse Bayesian dictionary learning; therefore ABPFA can achieve better recovery results for Aqua MODIS band 6. Although there is a very wide variance in reflectance types and the kinds of scenes in MODIS granules, this does not matter much for the recovery of ABPFA. Through our experiments, the geographic features are revealed well. In addition, the method does not introduce significant visual artifacts. Because the data we process are reflectances, even if the visual effect is pleasing, the subsequent and quantitative applications of Aqua MODIS band 6 (e.g., estimation of snow and cloud cover) are influenced to some degree, fortunately, for ABPFA, the influence is slight.

IV. CONCLUSION

This paper proposed an algorithm to retrieve the dead pixel stripes of Aqua MODIS band 6 by an adaptive spectrum-weighted sparse Bayesian dictionary learning method–ABPFA–which was based on the flourishing theory of CS. The proposed method took the spectral correlations between band 6 and the other bands into account to weigh the spectral characteristics more effectively, as confirmed by the indexes of SSIM, CC, and PSNR in the simulated data, and NR in the real Aqua MODIS experiments. The experimental results demonstrated that the proposed approach performed well. Although the complexity of ABPFA was high, because of the ever-growing computational capabilities, the computational cost may become secondary in importance to the improved performance. On the whole, ABPFA provided Aqua MODIS band 6 with a competitive method to recover the detectors' failure without regard to land cover types and spectral features. Many subsequent quantitative applications, such as the calculation of NDSI, the normalized difference infrared index [46], and aerosol optical depths [47], could benefit from it. However, for other problems (e.g., saturated pixels and sun glint), further research was still needed.

REFERENCES

[1] P. Rakwatin, W. Takeuchi, and Y. Yasuoka, "Restoration of Aqua MODIS band 6 using histogram matching and local least squares fitting," *IEEE Trans. Geosci. Remote Sens.*, vol. 47, no. 2, pp. 613–627, Feb. 2009.

[2] L. Wang, J. J. Qu, X. Xiong, X. Hao, and Y. Xie, "A new method for retrieving band 6 of Aqua MODIS," *IEEE Geosci. Remote Sens. Lett.*, vol. 3, no. 2, pp. 267–270, Apr. 2006.

[3] I. Gladkova, M. D. Grossberg, F. Shahriar, G. Bonev, and P. Romanov, "Quantitative restoration for MODIS band 6 on Aqua," *IEEE Trans. Geosci. Remote Sens.*, vol. 50, no. 6, pp. 2409–2416, Jun. 2012.

[4] H. Shen, C. Zeng, and L. Zhang, "Recovering reflectance of AQUA MODIS band 6 based on within-class local fitting," *IEEE J. Sel. Topics Appl. Earth Observat. Remote Sens.*, vol. 4, no. 1, pp. 185–192, Mar. 2011.

[5] M. Bertalmio, G. Sapiro, V. Caselles, and C. Ballester, "Image inpainting," in *Proc. 27th Int. Conf. Comput. Graph. Interact. Tech.*, Jul. 2000, pp. 417–424.

[6] A. C. Kokaram, R. D. Morris, W. J. Fitzgerald, and P. J. W. Rayner, "Interpolation of missing data in image sequences," *IEEE Trans. Image Process.*, vol. 4, no. 11, pp. 1509–1519, Nov. 1995.

[7] T. K. Shih, R.-C. Chang, L.-C. Lu, W.-C. Ko, and C.-C. Wang, "Adaptive digital image inpainting," in *Proc. 18th Int. Conf. Adv. Inf. Netw. Appl.*, vol. 1. 2004, pp. 71–76.

[8] M. Bertalmio, "Strong-continuation, contrast-invariant inpainting with a third-order optimal PDE," *IEEE Trans. Image Process.*, vol. 15, no. 7, pp. 1934–1938, Jul. 2006.

[9] H. Grossauer, "A combined PDE and texture synthesis approach to inpainting," in *Proc. 8th Eur. Conf. Comput. Vis.*, vol. 4. 2004, pp. 214–224.

[10] T. F. Chan, A. M. Yip, and F. E. Park, "Simultaneous total variation image inpainting and blind deconvolution," *Int. J. Imag. Syst. Technol.*, vol. 15, no. 1, pp. 92–102, Jul. 2005.

[11] M. K. Ng, H. Shen, S. Chaudhuri, and A. C. Yau, "Zoom-based super-resolution reconstruction approach using prior total variation," *Opt. Eng.*, vol. 46, no. 12, pp. 127003-1–127003-11, Dec. 2007.

[12] M. K. Ng, H. Shen, E. Y. Lam, and L. Zhang, "A total variation regularization based super-resolution reconstruction algorithm for digital video," *EURASIP J. Adv. Signal Process.*, vol. 2007, pp. 1–15, Jun. 2007.

[13] Y. Wei, S. Ji-Xiang, Z. Gang, T. Shuhua, and W. Gong-Jian, "PDE image inpainting with texture synthesis based on damaged region classification," in *Proc. 2nd Int. Conf. Adv. Comput. Control*, vol. 5. Mar. 2010, pp. 447–450.

[14] H. Shen and L. Zhang, "A MAP-based algorithm for destriping and inpainting of remotely sensed images," *IEEE Trans. Geosci. Remote Sens.*, vol. 47, no. 5, pp. 1492–1502, May 2009.

[15] H. Shen, Y. Liu, T. Ai, Y. Wang, and B. Wu, "Universal reconstruction method for quality improvement of remote sensing images," *Int. J. Appl. Earth Observat. Geoinf.*, vol. 12, no. 4, pp. 278–286, Aug. 2010.

[16] C. Jiang, H. Zhang, H. Shen, and L. Zhang, "A practical compressed sensing-based pan-sharpening method," *IEEE Geosci. Remote Sens. Lett.*, vol. 9, no. 4, pp. 629–633, Jul. 2012.

[17] L. Xiaoyan, Z. Jun, Y. Jingyu, and Q. Dai, "Image fusion in compressed sensing," in *Proc. 16th IEEE Int. Conf. Image Process.*, Nov. 2009, pp. 2205–2208.

[18] T. Wimalajeewa, C. Hao, and P. K. Varshney, "Performance limits of compressive sensing-based signal classification," *IEEE Trans. Signal Process.*, vol. 60, no. 6, pp. 2758–2770, Jul. 2012.

[19] L. Li and P. Fieguth, "Texture classification using compressed sensing," in *Proc. 7th Can. Conf. Comput. Robot Vis.*, Jun. 2010, pp. 71–78.

[20] L. Chengbo, S. Ting, K. F. Kelly, and Y. Zhang, "A compressive sensing and unmixing scheme for hyperspectral data processing," *IEEE Trans. Image Process.*, vol. 21, no. 3, pp. 1200–1210, Mar. 2012.

[21] M. D. Iordache, J. M. Bioucas-Dias, and A. Plaza, "Sparse unmixing of hyperspectral data," *IEEE Trans. Geosci. Remote Sens.*, vol. 49, no. 6, pp. 2014–2039, Jun. 2011.

[22] M. J. Fadili and J. L. Starck, "EM algorithm for sparse representation-based image inpainting," in *Proc. 12th IEEE Int. Conf. Image Process.*, vol. 2. Sep. 2005, pp. 61–64.

[23] Z. Mingyuan, C. Haojun, J. Paisley, R. Lu, L. Lingbo, X. Zhengming, D. Dunson, G. Sapiro, and L. Carin, "Nonparametric bayesian dictionary learning for analysis of noisy and incomplete images," *IEEE Trans. Image Process.*, vol. 21, no. 1, pp. 130–144, Jan. 2012.

[24] S. Bin, H. Wei, Z. Yimin, and Y.-J. Zhang, "Image inpainting via sparse representation," in *Proc. 34th IEEE Int. Conf. Acoust., Speech Signal Process.*, Apr. 2009, pp. 697–700.

[25] R. G. Baraniuk, "Compressive sensing," *IEEE Signal Process. Mag.*, vol. 24, no. 4, pp. 118–124, Jul. 2007.

[26] I. Tosic and P. Frossard, "Dictionary learning," *IEEE Signal Process. Mag.*, vol. 28, no. 2, pp. 27–38, Mar. 2011.

[27] D. L. Donoho, "Compressed sensing," *IEEE Trans. Inf. Theory*, vol. 52, no. 4, pp. 1289–1306, Apr. 2006.

[28] E. Candes and T. Tao, "Near optimal signal recovery from random projections: Universal encoding strategies?," *IEEE Trans. Inf. Theory*, vol. 52, no. 12, pp. 5406–5425, Dec. 2006.

[29] E. Candes, J. Romberg, and T. Tao, "Stable signal recovery from incomplete and inaccurate measurements," *Commun. Pure Appl. Math.*, vol. 59, no. 8, pp. 1207–1223, Aug. 2006.

[30] P. S. Huggins and S. W. Zucker, "Greedy basis pursuit," *IEEE Trans. Signal Process.*, vol. 55, no. 7, pp. 3760–3772, Jul. 2007.

[31] J. A. Tropp and A. C. Gilbert, "Signal recovery from random measurements via orthogonal matching pursuit," *IEEE Trans. Inf. Theory*, vol. 53, no. 12, pp. 4655–4666, Dec. 2007.

[32] D. Needell and R. Vershynin, "Uniform uncertainty principle and signal recovery via regularized orthogonal matching pursuit," *Found. Comput. Math.*, vol. 9, no. 3, pp. 317–334, Apr. 2009.

[33] W. Dai and O. Milenkovic, "Subspace pursuit for compressive sensing signal reconstruction," *IEEE Trans. Inf. Theory*, vol. 55, no. 5, pp. 2230–2249, May 2009.

[34] D. Needell and J. A. Tropp, "CoSaMP: Iterative signal recovery from incomplete and inaccurate samples," *Appl. Comput. Harmon. Anal.*, vol. 26, no. 3, pp. 301–321, 2009.

[35] M. Aharon, M. Elad, and A. Bruckstein, "K-SVD: An algorithm for designing overcomplete dictionaries for sparse representation," *IEEE Trans. Signal Process.*, vol. 54, no. 11, pp. 4311–4322, Nov. 2006.

[36] M. Elad and M. Aharon, "Image denoising via Sparse and Redundant representations over learned dictionaries," *IEEE Trans. Signal Process.*, vol. 15, no. 12, pp. 3736–3745, Dec. 2006.

[37] J. Mairal, F. Bach, J. Ponce, and G. Sapiro, "Online dictionary learning for sparse coding," in *Proc. 26th Annu. Int. Conf. Mach. Learn.*, 2009, pp. 689–696.

[38] M. Zhou, H. Chen, J. Paisley, L. Ren, G. Sapiro, and L. Carin, "Nonparametric Bayesian dictionary learning for sparse image representations," in *Proc. 23rd Annu. Conf. Neural Inf. Process. Syst.*, 2009, pp. 1–9.

[39] J. Paisley and L. Carin, "Nonparametric factor analysis with beta process priors," in *Proc. 26th Annu. Int. Conf. Mach. Learn.*, 2009, pp. 777–784.

[40] Z. Xing, M. Zhou, A. Castrodad, G. Sapiro, and L. Carin, "Dictionary learning for noisy and incomplete hyperspectral images," *SIAM J. Imag. Sci.*, vol. 5, no. 1, pp. 33–56, Jan. 2012.

[41] D. Knowles and Z. Ghahramani, "Infinite sparse factor analysis and infinite independent components analysis," *Independ. Compon. Anal. Signal Separat.*, vol. 4666, pp. 381–388, Sep. 2007.

[42] Y. W. Teh, "Dirichlet process," in *Encyclopedia of Machine Learning*. New York, USA: Springer-Verlag, 2010, pp. 280–287.

[43] W. Zhou and A. C. Bovik, "A universal image quality index," *IEEE Signal Process. Lett.*, vol. 9, no. 3, pp. 81–84, Mar. 2002.

[44] W. Zhou, A. C. Bovik, H. R. Sheikh, and E. P. Simoncelli, "Image quality assessment: From error visibility to structural similarity," *IEEE Trans. Image Process.*, vol. 13, no. 4, pp. 600–612, Apr. 2004.

[45] A. Cherian, S. Sra, and N. Papanikolopoulos, "Denoising sparse noise via online dictionary learning," in *Proc. 36th IEEE Int. Conf. Acoust. Speech Signal Process.*, May 2011, pp. 2060–2063.

[46] E. R. Hunt, Jr., L. Li, M. T. Yilmaz, and T. J. Jackson, "Comparison of vegetation water contents derived from shortwave-infrared and passive-microwave sensors over central Iowa," *Remote Sens. Environ.*, vol. 115, no. 9, pp. 2376–2383, 2011.

[47] A. Ignatov, P. Minnis, N. Loeb, B. Wielicki, W. Miller, S. Sun-Mack, D. Tanre, L. Remer, and I. Laszlo, "Two MODIS aerosol products over ocean on the terra and aqua ceres ssf datasets," *J. Atmospheric Sci.*, vol. 62, no. 4, pp. 1008–1031, 2005.

Huanfeng Shen (M'11) received the B.S. degree in surveying and mapping engineering and the Ph.D. degree in photogrammetry and remote sensing from Wuhan University, Wuhan, China, in 2002 and 2007, respectively.

He joined the School of Resource and Environmental Science, Wuhan University, in July 2007, where he is currently a Full Professor. He has been supported by several talent programs, including the New Century Excellent Talents by the Ministry of Education of China in 2011, and the Hubei Science Fund for Distinguished Young Scholars in 2011. He has published more than 60 research papers. His current research interests include image processing (for quality improvement), remote sensing application, data fusion, and assimilation.

Xinghua Li received the B.S. degree in geographical information system from Wuhan University, Wuhan, China, in 2011. He is currently pursuing the Ph.D. degree with the School of Resource and Environmental Science, Wuhan University.

His current research interests include image inpainting and compressed sensing based image processing.

Liangpei Zhang (M'06–SM'08) received the B.S. degree in physics from Hunan Normal University, Changsha, China, in 1982, the M.S. degree in optics from the Xi'an Institute of Optics and Precision Mechanics of Chinese Academy of Sciences, Xi'an, China, in 1988, and the Ph.D. degree in photogrammetry and remote sensing from Wuhan University, Wuhan, China, in 1998.

He is currently with the State Key Laboratory of Information Engineering in Surveying, Mapping and Remote Sensing, Wuhan University, as the Head of the Remote Sensing Division. He is a "Chang-Jiang Scholar" Chair Professor appointed by the Ministry of Education, China. He has more than 260 research papers and five patents. He is currently a Principal Scientist with the China State Key Basic Research Project from 2011 to 2016 appointed by the Ministry of National Science and Technology of China to lead the remote sensing program in China. His current research interests include hyperspectral remote sensing, high resolution remote sensing, image processing, and artificial intelligence.

Dr. Zhang serves as an Associate Editor of the IEEE TRANSACTIONS ON GEOSCIENCE AND REMOTE SENSING, the *International Journal of Ambient Computing and Intelligence*, the *International Journal of Image and Graphics*, the *International Journal of Digital Multimedia Broadcasting*, the *Journal of Geospatial Information Science*, and the *Journal of Remote Sensing*. He is fellow of the IEE, Executive member (Board of Governor) of the China National Committee of International Geosphere-Biosphere Programme, Executive member for the China Society of Image and Graphics. He regularly serves as a Co-Chair of the series SPIE Conferences on Multispectral Image Processing and Pattern Recognition, Conference on Asia Remote Sensing, and many other conferences. He edits several conference proceedings, issues, and the Geoinformatics Symposiums.

Dacheng Tao (M'07–SM'12) received the B.Eng. degree from the University of Science and Technology of China, Hefei, China, the M.Phil. degree from The Chinese University of Hong Kong, Hong Kong, and the Ph.D. degree from the University of London, London, U.K.

He is a Professor of computer science with the Centre for Quantum Computation and Information Systems and the Faculty of Engineering and Information Technology, University of Technology, Sydney, Australia. He mainly applies statistics and mathematics for data analysis problems in data mining, computer vision, machine learning, multimedia, and video surveillance. He has authored or co-authored more than 100 scientific articles at top venues, including the IEEE T-PAMI, T-KDE, T-IP, NIPS, ICML, UAI, AISTATS, ICDM, IJCAI, AAAI, CVPR, ECCV, ACM T-KDD, Multimedia, and KDD.

Prof. Tao was the recipient of the Best Theory/Algorithm Paper Runner Up Award in IEEE ICDM in 2007.

Chao Zeng received the B.S. degree in resources-environment and urban-rural planning management and the M.S. degree in surveying and mapping engineering from Wuhan University, Wuhan, China, in 2009 and 2011, respectively. He is currently pursuing the Ph.D. degree with the State Key Laboratory of Information Engineering in surveying, mapping, and remote sensing, Wuhan University.

His current research interests include remote sensing image processing and remote sensing applications.